scientific reports

OPEN

Hybridized bands and stacking-dependent band edges in ferromagnetic Fe_3GeTe_2/$CrGeTe_3$ moiré heterobilayer

Eunjung Ko

Owing to unique fundamental physics and device applications, twisted moiré physics in two-dimensional (2D) van der Waals (vdW) layered magnetic materials has recently received particular attention. We investigate magnetic vdW Fe_3GeTe_2 (FGT)/$CrGeTe_3$ (CGT) moiré heterobilayers with twist angles of 11° and 30° from first-principles. We show that the moiré heterobilayer is a ferromagnetic metal with an *n*-type CGT layer due to the dominant spin-majority electron transfer from the FGT layer to the CGT layer, regardless of various stacked structures. The spin-majority hybridized bands between Cr and Fe bands crossing the Fermi level are found regardless of stacking. The band alignment of the CGT layer depends on the effective potential difference at the interface. We show that an external electric field perpendicular to the in-plane direction modulates the interface dipole and band edges. Our study reveals a deeper understanding of the effects of stacking, spin alignment, spin transfer, and electrostatic gating on the 2D vdW magnetic metal/semiconductor heterostructure interface.

2D vdW layered metal–semiconductor nonmagnetic heterostructures have been studied for developing high-performance devices with the contact of metal electrodes and semiconductors[1–7]. Recently, heterostructures consisting of 2D ferromagnetic (FM) vdW layered materials have attracted considerable interest[8–10]. In particular, research on the 2D vdW heterobilayer composed of magnetic metals and magnetic semiconductors is still early, as it was only recently revealed that vdW monolayer (ML) or few-layer materials retain magnetism[11–13]. Furthermore, the recent discovery of novel properties of twisted vdW nonmagnetic homo and heterobilayers[14–16] further prompts the investigation of twisted vdW magnetic homo and heterobilayers.

Recent experiments have demonstrated the long-range 2D FM order along the out-of-plane direction in the metallic ML FGT[17–20] and the semiconducting CGT bilayer samples[21,22]. Thus, metallic Fe_3GeTe_2 (FGT) and semiconducting $CrGeTe_3$ (CGT) materials are promising candidates for forming low-dimensional heterobilayers. Several experimental works have reported that bulk FGT is an itinerant FM metal with a high Curie temperature, T_c, of approximately 230 K; T_c can be increased to room temperature by electrostatic gating and decreased by decreasing the layer thickness[17–20]. Theoretical studies have reported changes in the magnetic anisotropy energy (MAE), magnetic order from the bulk to ML, the anomalous Hall effect, and spin-dependent transport in tunnel junctions[10,23–26]. On the other hand, some experimental studies have revealed that bulk CGT is an intrinsic FM semiconductor with a T_c of 61 K[27] and an experimental bandgap, E_g, in the range 0.2–0.7 eV[28–31]. Several theoretical works have examined variations in T_c, magnetic order, MAE, and E_g from the bulk to ML[28,32–39]. Although each FGT and CGT has been thoroughly investigated, the basic properties of the FGT/CGT heterobilayer have not been fully explored. Moreover, there has not been much research on the twisted moiré heterobilayer of vdW magnetic metal/semiconductor materials[11]. Hence, it is worth examining the promising FGT/CGT twisted moiré heterobilayer.

The Schottky barrier heights at the interface between a metal and a semiconductor are crucial properties for device applications. They classify the heterostructure interface into a Schottky contact (*n*- or *p*-type) or an Ohmic contact. In general, the additional interface states caused by extra bonds at the interface facilitate the formation of Schottky contact[40,41], whereas they complicate that of Ohmic contact. Thus, the Schottky barrier heights at the metal–semiconductor interface with Schottky contact have been extensively studied. Experimental studies have reported converting a Schottky contact to an Ohmic contact by large gating voltages in 3D metal/2D vdW semiconductor heterostructures[42,43]. Meanwhile, the formation of extra bonds at the interface between 2D

Korea Institute for Advanced Study, Seoul 02455, Korea. email: eunjungko04@kias.re.kr

vdW materials can be prevented due to the vdW interlayer distance, and thus the heterostructure has an abrupt interface. Because of this advantage, the band edges of heterostructures combined with 2D vdW metals and semiconductors have been investigated with and without electrostatic gating for device applications. Several theoretical studies have shown the electrostatic gating effect on the band edges of nonmagnetic 2D vdW metal/semiconductor heterobilayers[1,5]. However, first-principles studies on the band edges of 2D vdW magnetic twisted moiré metal/semiconductor heterobilayers have rarely been performed[11].

In this work, we conducted a first-principles study on the structural, electronic, and magnetic properties of the FGT/CGT moiré heterobilayer with twist angles of 11° and 30°. First, we examined the atomic distortion and unfolded band structures in a large moiré supercell with a twist angle of 11°, and then investigated the band edges depending on stacking in a small moiré supercell with a twist angle of 30° with and without electrostatic gating. Each small moiré heterobilayer having one of six possible stacked structures was an FM metal with an *n*-type CGT layer, induced by the effective spin-majority electron transfer from FGT to CGT. We also compared the band structures of the FM and AFM heterobilayers, having FM and antiferromagnetic (AFM) spin alignments between FGT and CGT. We found that only the FM heterobilayer had the hybridized bands between the Cr and Fe atoms. Further, we explained the stacking-dependent band edges of the CGT layer in terms of the effective potential difference. Finally, we addressed the external electric field effect on the band edges of the CGT layer in the FM heterobilayer.

Methods

We conducted first-principles electronic structure computations using the noncollinear density functional theory (DFT) with the Hubbard repulsion, U, and exchange interaction, J, as well as the spin–orbit coupling (SOC). We used the norm-conserving pseudopotentials[44] with the SIESTA code[45]. We adopted the generalized-gradient approximation, parameterized by the Perdew–Burke–Ernzerhof (PBE) formula. Further, we used the rotationally invariant U approach[46] to describe the electron correlation for Cr 3*d* orbitals. The atomic structures were optimized using the spin-polarized optB88 vdW method until all atomic forces were less than 0.001 eV Å^{-1} except for a huge moiré supercell with a twist angle of 11°, where the force criteria were 0.036 eV Å^{-1}. In addition, we generated a semicore pseudopotential for Cr using the ($3s^2$, $3p^6$, $3d^5$, $4s^0$) valence configuration; the valence configurations for Fe, Ge, and Te pseudopotentials were ($3d^7$, $4s^1$, $4p^0$), ($3d^{10}$, $4s^2$, $4p^2$), and ($4d^{10}$, $5s^2$, $5p^4$), respectively. We generated real-space grids with a cutoff energy of 400 Ry and expanded the electronic wave functions using pseudoatomic orbitals (PAOs) of the double-zeta polarization basis set. We utilized a $16 \times 16 \times 1$ *k*-grid for all structure relaxation and electronic structure calculations except for a large moiré supercell with a twist angle of 11°, for which we applied a $2 \times 2 \times 1$ *k*-grid. For ML CGT, we obtained $U = 5.97$ eV and $J = 1.00$ eV for Cr 3*d* orbitals with a cutoff radius of 1.58 Å by using a PAO-based constrained DFT (cDFT) method[45,47]. However, our previous study confirmed that the suitable theoretical bandgap close to the experimental one was obtained by the PBE + U + SOC method using a U in the range of 3–4 eV and $J = 1$ eV[48]. Therefore, we selected $U = 3.5$ eV and $J = 1$ eV for our calculations. To remove the interactions between FGT and CGT, we applied a vacuum space of 16 Å.

Results and discussion

Twisted FGT/CGT moiré heterobilayer. Bulk FGT has a layered hexagonal structure with space group $P6_3/mmc$ and experimental hexagonal cell parameters $a = b = 4.030$ and 3.991 Å and $c = 16.343$ and 16.336 Å from refs. 47 and 48, respectively. In ML FGT, each unit cell contains three Fe atoms occupying two nonequivalent Fe positions; Fe1 and Fe2 denote the relevant atoms. ML FGT consists of five sublayers: the first and fifth are occupied by Te atoms, the second and fourth by Fe1 atoms, and the third by Fe2 and Ge atoms. Our relaxed lattice constants for pristine ML FGT that are obtained using the spin-polarized optB88 vdW method are $a = b = 4.091$ Å. Bulk CGT has a rhombohedral symmetry with space group $R\bar{3}$ and experimental hexagonal cell parameters $a = b = 6.8196$ Å and $c = 20.3710$ Å at 5 K[27]. ML CGT has two Cr atoms in a unit cell. ML CGT consists of five sublayers: the first and fifth are occupied by Te atoms, the second and fourth by Ge atoms, and the third by Cr atoms. ML CGT has a honeycomb lattice of edge-sharing $CrTe_6$ octahedrons, and Ge dimers located at the center of the hexagon. Our relaxed lattice constants for pristine ML CGT that are obtained using the spin-polarized optB88 vdW method are $a = b = 6.940$ Å. The point group for ML FGT and ML CGT is D_{3h} and C_1, respectively. Thus the heterobilayer built by ML FGT and ML CGT has the C_1 symmetry.

The heterobilayer of ML FGT and ML CGT has a moiré pattern due to the lattice mismatch. In principle, the twist angle ϕ between the supercell lattice vectors of the FGT and CGT layers for a moiré supercell (i.e., ϕ between $\overrightarrow{L}_{\mathrm{CGT},1}$ and $\overrightarrow{L}_{\mathrm{FGT},1}$ in Fig. 1a) is the same as that between the unit vectors of ML FGT and ML CGT. Hence, the moiré reciprocal lattice vector, $\overrightarrow{k}_{\mathrm{moiré}}$, and the moiré wavelength, λ, can be easily obtained as $\vec{k}_{\mathrm{moiré}} = \vec{k}_{\mathrm{FGT}} - \vec{k}_{\mathrm{CGT}}$ and $\lambda = \frac{2\pi}{\left|\vec{k}_{\mathrm{moiré}}\right|}$, respectively, using reciprocal lattice vectors corresponding to the unit cell vectors. Concretely, when the unit vectors of ML CGT are $\overrightarrow{a}_1 = a\left(\frac{\sqrt{3}}{2}, -\frac{1}{2}\right)$ and $\overrightarrow{a}_2 = a\left(\frac{\sqrt{3}}{2}, \frac{1}{2}\right)$, and the unit vectors of ML FGT are rotated by ϕ relative to those of ML CGT, the reciprocal lattice vectors become $\overrightarrow{k}_{\mathrm{CGT}} = \frac{2\pi}{a}(1, 0)$ for ML CGT and $\overrightarrow{k}_{\mathrm{FGT}} = \frac{2\pi}{a(1-\delta)}(cos\phi, sin\phi)$ for ML FGT, where $\delta = 1 - a_{\mathrm{FGT}}/a_{\mathrm{CGT}}$ as shown in the left panel in Fig. 1a. Thus, the moiré wavelength, λ, becomes $\lambda = \frac{2\pi}{\left|\vec{k}_{\mathrm{moiré}}\right|} = (1-\delta)a/\sqrt{2(1-\delta)(1-cos\phi)+\delta^2}$[49,50]. The right panel in Fig. 1a shows λ (red lines) with respect to the twist angle ϕ between ML CGT and ML FGT optimized using the spin-polarized optB88 vdW method. The moiré superlattice vectors can be expressed as $\overrightarrow{L}_{\mathrm{CGT},1} = m\overrightarrow{a}_1 + n\overrightarrow{a}_2$ and $\overrightarrow{L}_{\mathrm{CGT},2} = -n\overrightarrow{a}_1 + (m+n)\overrightarrow{a}_2$ for ML CGT and $\overrightarrow{L}_{\mathrm{FGT},1} = p\overrightarrow{b}_1 + q\overrightarrow{b}_2$ and

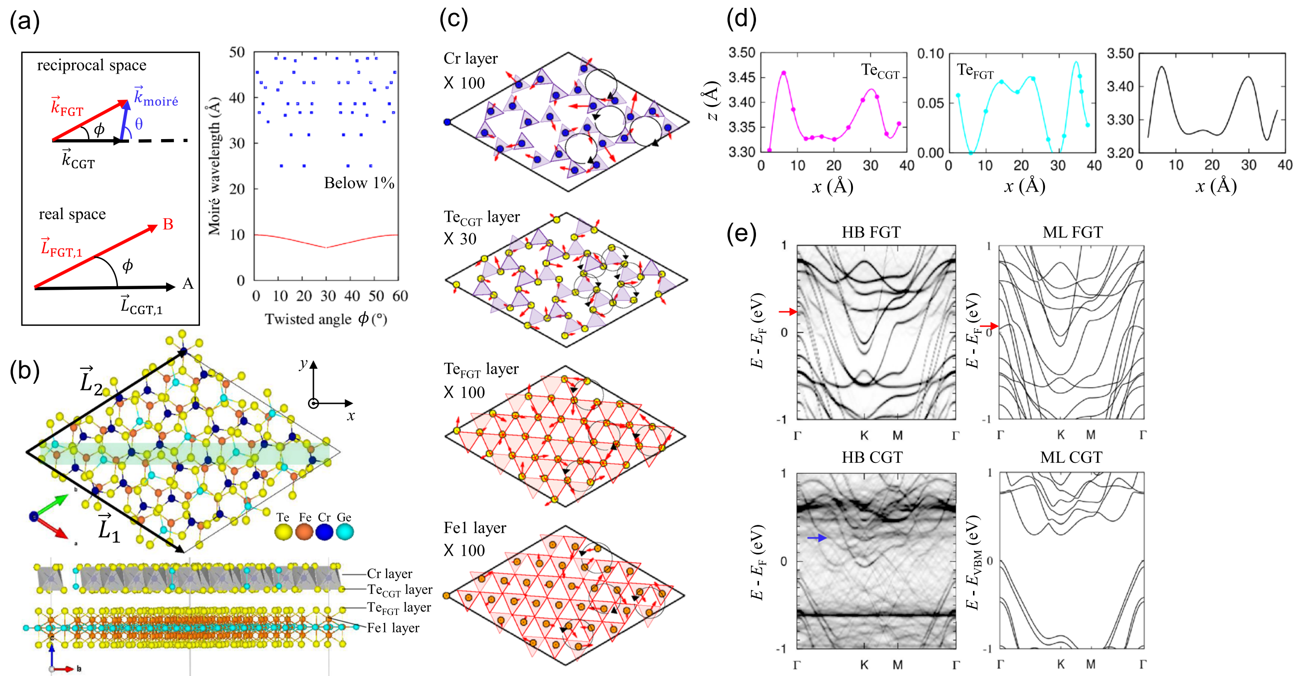

Figure 1. (**a**) $\vec{k}$ wave vectors of monolayer (ML) Fe_3GeTe_2 (FGT) and ML $CrGeTe_3$ (CGT) in reciprocal space, moiré lattice vectors in real space (left panel), and moiré wavelength as a function of twist angles (red lines, right panel). (**b**) Top and side views of twisted moiré lattice with a moiré lattice constant of 25.02 Å, a lattice mismatch Δ of 0.55%, a twist angle ϕ of 11.39°, and $(m, n, p, q) = (1, 3, 3, 4)$. Only Fe1, Te_{FGT}, Te_{CGT}, Ge_{CGT}, and Cr atoms near the interface are depicted in the top view. (**c**) In-plane displacement vectors (red arrows) of Cr, Te_{CGT}, Te_{FGT}, and Fe1 layers. The atomic structures are obtained using the spin-polarized optB88 vdW method. The red arrows are enlarged to 30 or 100 times their original size. The purple (red) triangles comprise the interface Te_{CGT} (Te_{FGT}) atoms. (**d**) *Z*-coordinates of interface Te atoms along a diagonal in the *x*-axis (left and middle panels) and interlayer distance between Te_{FGT} and Te_{CGT} atoms (right panel). (**e**) Unfolded band structures of moiré heterobilayer calculated by the noncollinear PBE + U + SOC method when $U = 3.5$ eV and $J = 1.0$ eV. They are drawn along the unit-cell bandlines of FGT (HB_FGT) and CGT (HB_CGT). The moiré heterobilayer has a ferromagnetic (FM) spin alignment between the FGT and CGT layers. For comparison, the band structures of ML FGT and ML CGT are shown. The red and blue arrows indicate differences between the moiré heterobilayer and the monolayer.

$\vec{L}_{FGT,2} = -q\vec{b}_1 + (p+q)\vec{b}_2$ for ML FGT, where m, n, p, and q are integers. We can obtain the commensurate moiré lattice vectors by applying a small biaxial strain Δ between ML CGT and ML FGT layers. Δ is estimated by $\Delta = |a\sqrt{m^2+n^2+mn} - b\sqrt{p^2+q^2+pq}|(b\sqrt{p^2+q^2+pq})^{-1}$. The moiré wavelengths within the constrained condition of Δ being less than 1.0% are shown as blue squares in the right panel in Fig. 1a. Here the twist angle ϕ is determined as $cos\phi = \left(\left|\vec{L}_{CGT,1}\right|^2 + \left|\vec{L}_{FGT,1}\right|^2 - |\overline{AB}|^2\right)\left(2\left|\vec{L}_{CGT,1}\right|\left|\vec{L}_{FGT,1}\right|\right)^{-1}$, where $|\overline{AB}| = \left|\vec{L}_{CGT,1} - \vec{L}_{FGT,1}\right| = |m\vec{a}_1 + n\vec{a}_2 - p\vec{b}_1 - q\vec{b}_2|$[51].

Figure 1b displays the top and side views of the moiré superlattice with $\lambda = 25.02$ Å, $\Delta = 0.55\%$, $\phi = 11.39°$, $(m, n, p, q) = (1, 3, 3, 4)$, and the total number of atoms being 352. Only Fe1, Te_{FGT}, Te_{CGT}, Ge_{CGT}, and Cr atoms near the interface are depicted in the top view of Fig. 1b. The moiré supercell has $CrTe_6$ hexagonal networks on top of FGT and various stacked structures. The in-plane and out-of-plane distortions obtained by the spin-polarized optB88 vdW method are displayed in Fig. 1c,d, respectively. The in-plane displacement vectors indicated by red arrows show more in-plane distortion in CGT than in FGT and are largest at the Te_{CGT} layer. In particular, the in-plane displacement vectors of all Te_{CGT} atoms have consistent patterns regardless of stacking, as depicted by black circles, but those of other atoms vary depending on stacking. The *z*-coordinates of Te_{CGT} and Te_{FGT} atoms inside the green shaded region in (b) vary depending on stacking, as shown in Fig. 1d. The out-of-plane distortion of the Te_{CGT} layer is much larger than that of the Te_{FGT} layer. The variation of interlayer distance between two interface Te layers is largest in the area where Te_{CGT} atoms are closely located above Te_{FGT} atoms.

The unfolded band structures of the moiré heterobilayer with a twist angle of 11.39° reveal some distinct features compared with the unit-cell band structures of a single layer, as shown in Fig. 1e. All the band structures were obtained using the noncollinear PBE + U + SOC method when $U = 3.5$ eV and $J = 1.0$ eV for Cr 3*d* orbitals, and an FM spin alignment between FGT and CGT was considered. The average magnetic moment is 3.64 μ_B/atom for Cr, 2.61 μ_B/atom for Fe1, and 1.65 μ_B/atom for Fe2. The unfolded band structures of FGT (HB FGT) near the Fermi level are similar to the unit-cell band structures of ML FGT except for bands shifted higher in

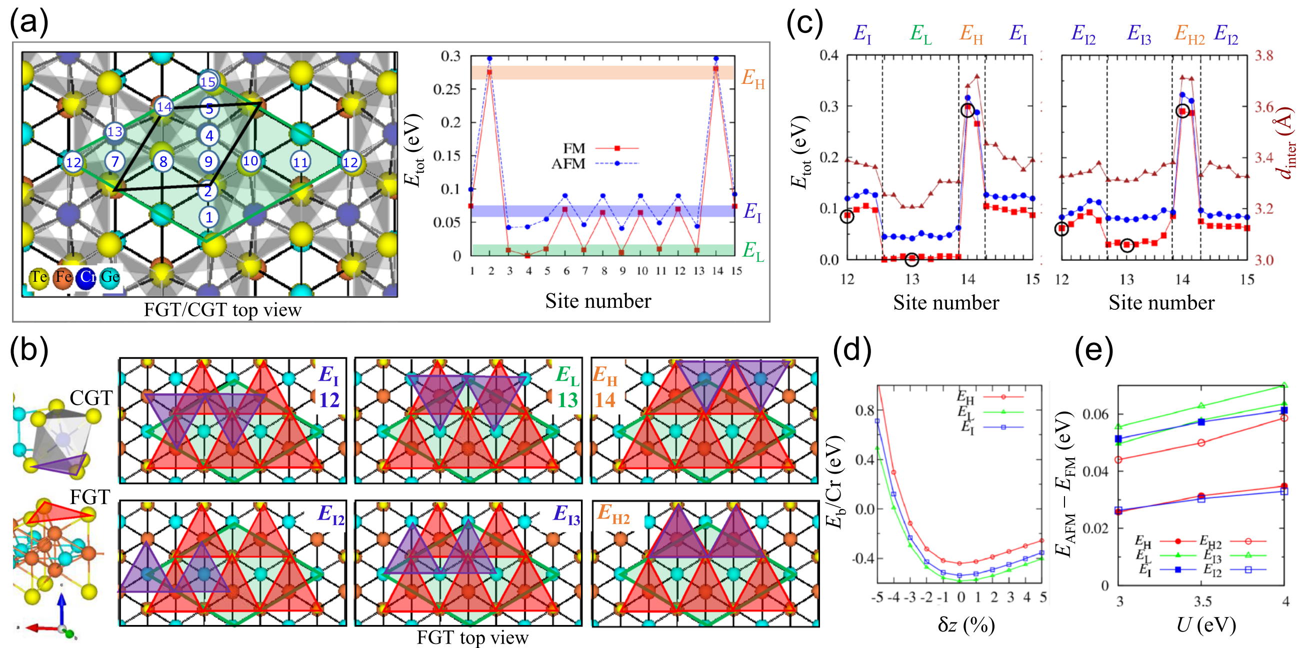

Figure 2. (**a**) Top view of FGT/CGT moiré supercell with a twist angle of 30° (green diamond) in the left panel, and total energy comparison of 15 stacked structures with the ferromagnetic (FM)/antiferromagnetic (AFM) spin alignment between the FGT and CGT layers in the right panel. The calculations are done using the spin-polarized optB88 vdW method. The supercell size is the same as the in-plane ML CGT unit cell size. A black diamond indicates the in-plane ML FGT unit cell. The numbered sites along two diagonals and one in-plane lattice indicate 15 stacked structures. The 15 stacked structures were made by sliding CGT over the numbered sites while FGT was fixed. The FM total energy is classified into three energies: E_I, E_L, and E_H. (**b**) Six representative stacked structures of E_I (site 12), E_L (site 13), E_H (site 14), E_{I2}, E_{I3}, and E_{H2}. The background lattice shows the FGT top view. The red (purple) triangles comprise the interface Te_{FGT} (Te_{CGT}) atoms. Two purple triangles are situated above $Fe1_{FGT}$ atoms for E_I, Ge_{FGT} atoms for E_L, and Te_{FGT} atoms for E_H. E_{I2}, E_{I3}, and E_{H2} are obtained by rotating the CGT layer 180° and relaxing it. (**c**) FM/AFM total energy variation from E_I (E_{I2}) through E_L (E_{I3}) to E_H (E_{H2}) representative structures with FM/AFM spin alignment and the interlayer distance, d_{inter}, depending on FM stacked structures. The total energy and structures are obtained using the spin-polarized optB88 vdW method. The red, blue, and brown colors indicate FM, AFM, and d_{inter}, respectively. (**d**) Binding energy, E_b, per Cr atom of E_H, E_L, and E_I along the z-axis regarding small displacements. (**e**) Total energy difference between FM and AFM spin alignments obtained by using the noncollinear PBE + U + SOC method, when U is in the range 3–4 eV and the exchange interaction is J = 1.0 eV.

energy denoted by red arrows. On the other hand, the unfolded band structures of CGT (HB CGT) exhibit a reduced bandgap compared with that of ML CGT, and the conduction bands of HB CGT cross the Fermi level, generating an n-type CGT layer. Also, unexpected bands of HB CGT are observed as indicated by a blue arrow compared to ML CGT. These intriguing electronic features of moiré heterobilayer motivate us to examine the critical elements that influence band structures.

To investigate the electronic structures in terms of stacked structures, we constructed small moiré supercells of the FGT/CGT heterobilayer forming only one stacked structure with a twist angle of 30° and $\Delta = 1.36\%$, as shown in Fig. 2a. The in-plane supercell indicated by a solid green diamond is equal to the 1×1 in-plane unit cell of ML CGT and also corresponds to the 30° rotated $\sqrt{3} \times \sqrt{3}$ in-plane supercell of ML FGT, drawn by an open black diamond. Inside the supercell, there are two $CrTe_6$ octahedrons.

ML FGT is an Ising-type FM metal, whereas ML CGT is an Ising-type FM semiconductor. To predict the magnetic structures of the heterobilayer, we compared the total energy of the heterobilayer with the FM and antiferromagnetic (AFM) spin alignments between ML FGT and ML CGT along the direction perpendicular to the interface. As shown in the left panel in Fig. 2a, we considered 15 different stacked structures while fixing ML FGT and sliding ML CGT. Concretely, we considered six different stacked structures in two diagonal directions of the in-plane supercell and three different stacked structures in the direction of the in-plane lattice. All the atoms were optimized during the relaxation in the x-, y-, and z-directions. The FM spin alignment between ML FGT and ML CGT always has lower energy than the AFM spin alignment at each stacked structure, as shown in the right panel in Fig. 2a.

We categorized the FM energy into three classes: the lowest, E_L, intermediate, E_I, and the highest energy, E_H. The corresponding stacked structures are depicted in the top panel in Fig. 2b. The background lattice shows the FGT top view. The red and purple triangles represent the interface Te triangles in the FGT and CGT layers, respectively. We drew two purple triangles on the bottom Te atoms in CGT related to two $CrTe_6$ octahedrons inside a supercell. In the E_I structure, the interface Te_{CGT} atom is above the $Fe1_{FGT}$ atom; in the E_L structure, it is above the Ge_{FGT} atom; and, in the E_H structure, it is located above the interface Te_{FGT} atom. Three more possible

CGT	ML	E_I	E_L	E_H	E_{I2}	E_{I3}	E_{H2}
a (Å)	6.94	7.06	7.07	7.06	7.06	7.06	7.06
(%)		1.75	1.82	1.76	1.79	1.79	1.78
FGT	**ML**	E_I	E_L	E_H	E_{I2}	E_{I3}	E_{H2}
a (Å)	4.09	4.08	4.08	4.08	4.08	4.08	4.08
(%)		−0.33	−0.27	−0.33	−0.28	−0.28	−0.29

Table 1. Lattice constant variation in the FM heterobilayer with a twist angle of 30°. During the relaxation of the heterobilayer, the lattice constants of CGT and FGT become tensile strained and compressive strained, respectively.

stacked structures illustrated in the bottom panel were examined; the purple triangle consisting of interface Te_{CGT} atoms was rotated 180° relative to those in the top panel. Two more intermediate energy structures, E_{I2} and E_{I3}, and another highest energy structure, E_{H2}, were found. In E_{I2}, E_{I3}, and E_{H2} structures, the interface Te_{CGT} atom is above the $Fe1_{FGT}$, Ge_{FGT}, and Te_{FGT} atoms, respectively.

Figure 2c presents the total energy difference with the FM (red) and AFM (blue) spin alignments, as well as the interlayer distance (brown) between the interface Te atoms of the FM structures. All the atoms and axes were optimized during the relaxation in the *x*-, *y*-, and *z*-directions using the spin-polarized optB88 vdW method. The total energy difference changes gradually from E_I through E_L to E_H (left panel) and from E_{I2} through E_{I3} to E_{H2} (right panel). The total energy difference and the interlayer distance are the smallest for E_L and the largest for E_H and E_{H2}. E_I, E_L, E_H, E_{I2}, E_{I3}, and E_{H2} structures have interlayer distances of 3.39 Å, 3.22 Å, 3.78 Å, 3.33 Å, 3.31 Å, and 3.71 Å, respectively. At each FM heterobilayer, the lattice constants of the CGT and FGT layers become tensile strained and compressive strained, respectively, as summarized in Table 1. The total energy of FM spin alignment is lower than that of AFM for E_I, E_L, E_H, E_{I2}, E_{I3}, and E_{H2} by 0.02 eV, 0.04 eV, 0.02 eV, 0.02 eV, 0.05 eV, and 0.03 eV, respectively. At the FM spin alignment, the total energy of the E_L structure is lower than that of E_I, E_H, E_{I2}, E_{I3}, and E_{H2} structures by 0.08 eV, 0.30 eV, 0.06 eV, 0.03 eV, and 0.29 eV, respectively. Figure 2d shows the binding energy, E_b, per Cr atom along the *z*-direction regarding the small displacement. At the equilibrium position, the binding energy per Cr atom obtained using the spin-polarized optB88 vdW method has a negative value of − 0.44 eV, − 0.58 eV, and − 0.54 eV for E_H, E_L, and E_I, respectively. The lower the total energy is, the lower the binding energy is. In the PBE + U + SOC method, the FM spin alignment also has lower energy than the AFM spin alignment when U is 3–4 eV and $J = 1$ eV for all the stacked structures, as shown in Fig. 2e.

The band alignment of FM and AFM heterobilayers was investigated. Figure 3 shows the magnetic moment (left panels), spin-majority (up) and spin-minority (down) band structures (middle panels), and atom projected density of states (PDOS, right panels) of (a) the FM CGT-only system, (b) FM FGT-only system, (c) FM FGT/CGT heterobilayer for E_H, and (d) AFM FGT/CGT heterobilayer for E_H in the supercell band lines. The band structures were calculated by using the noncollinear PBE + U + SOC method on Cr 3*d* orbitals with $U = 3.5$ eV and $J = 1.0$ eV. It should be noted that the CGT (FGT)-only system refers to only the CGT (FGT) layer and no FGT (CGT) layer while maintaining the relaxed heterobilayer structures. The band projections onto the spin-up and spin-down bands of Cr or Fe atoms are distinguished by red and blue colors, respectively, with various color intensities proportional to the projection magnitude to examine the band alignment. The semiconducting bandgap of 0.43 eV is shown for a Cr atom in the FM CGT-only system (Fig. 3a), while the metallic band structure is shown for a Fe2 atom in the FM FGT-only system (Fig. 3b). The magnetic moment is 3.69 μ_B/atom for Cr, 2.62 μ_B/atom for Fe1, and 1.67 μ_B/atom for Fe2. The atom PDOS of a Fe2 atom in (b) indicates an equivalent magnitude of spin-up and spin-down PDOS near the Fermi level. The CGT-only system features a conduction band minimum (CBM) at a k point between the Γ and K points dominated by spin-up empty Cr 3*d* e_g bands. Its valence band maximum (VBM) at the Γ point is dominated by Te 5*p* orbital characteristics, similar to the pristine ML CGT.

On the other hand, the heterobilayer formed by CGT- and FGT-only systems is an FM metal, as shown in Fig. 3c. The bands projected on a Cr atom show the initial Cr bands observed in the CGT-only system as well as unique spin-up hybridized bands with Fe2 bands crossing the Fermi level, as indicated by green and blue arrows, respectively. The hybridization is not related to Fe1 bands, as seen by the band projected on a Fe1 atom. Furthermore, when the hybridized spin-up bands are ignored, the CBM of Cr bands appears to be at the spin-down bands, located at an energy close to the Fermi level, generating an *n*-type CGT layer. The *n*-type CGT means that electrons are transferred from the FGT to CGT layers. In the right panel of Fig. 3c, the downward-band shifts of a Cr atom in the heterobilayer can be observed in the atom PDOS. The spin-up Fe2 bands shift higher in energy near the Γ point when the system switches from an FGT-only system to a heterobilayer, as indicated by the black arrows in (b) and (c). These upward shifted spin-up Fe2 bands might also originate from the electron transfer from the FGT to CGT layers. Unlike the FM heterobilayer, the AFM-heterobilayer-band structures do not exhibit hybridized bands between FGT and CGT bands but do expose an *n*-type CGT layer via the spin-up and spin-down CBM of the original Cr bands crossing the Fermi level. AFM heterobilayer, like FM heterobilayer, features shifted spin-down Fe2 bands near the Γ point that are higher in energy than those of the FGT-only system (black arrow in (d)), indicating electron transfer from the FGT to CGT layers.

Figure 4 shows the spin-up (red) and spin-down (blue) band structures projected on a Cr atom of all the stacked structures with the FM spin alignment. All the band structures exhibit spin-up hybridized bands crossing

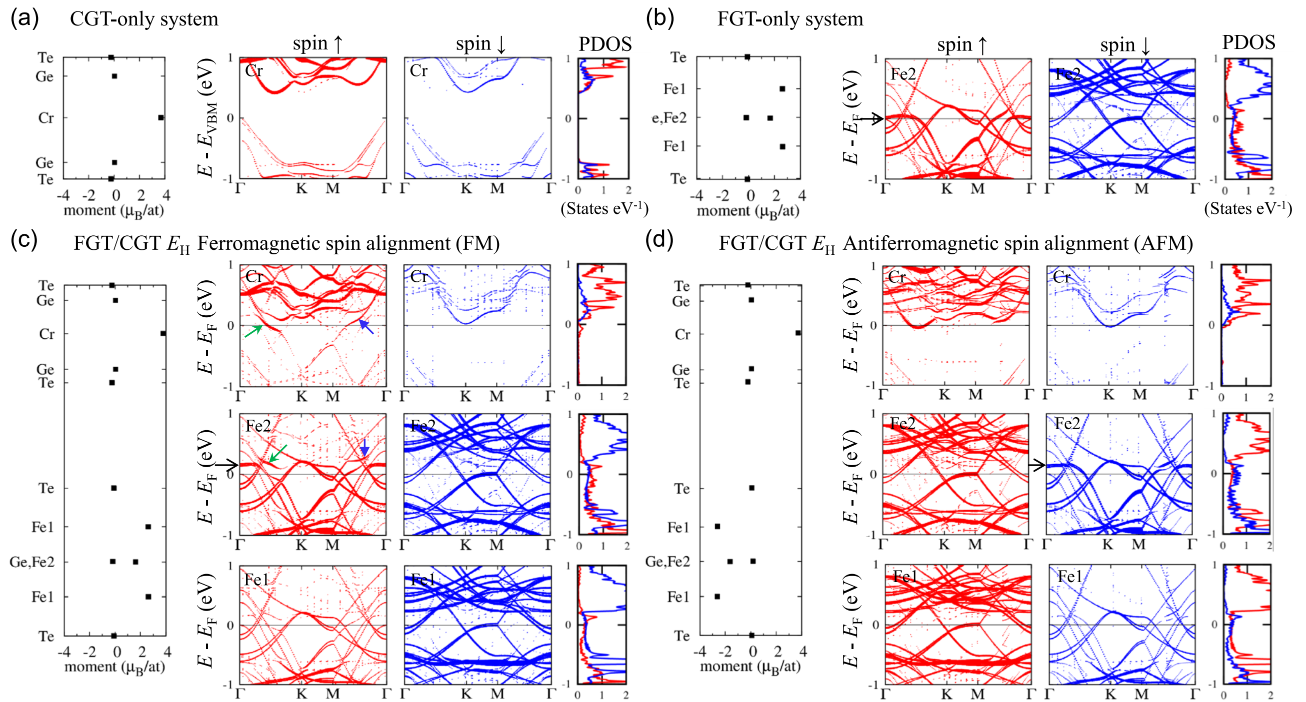

Figure 3. Magnetic moment (left panels), projected band structures (middle panels), and atom projected density of states (PDOS, right panels) of (**a**) the CGT-only system, (**b**) FGT-only system, (**c**) FM FGT/CGT heterobilayer of E_H, and (**d**) AFM FGT/CGT heterobilayer of E_H. The band structures are obtained by the noncollinear PBE + U + SOC method (U = 3.5 eV and J = 1.0 eV applied to Cr 3d orbitals). The band structures are projected onto a Cr or Fe atom; the color intensity corresponds to the projection magnitude. In (**c**), green and blue arrows indicate the hybridized bands between Cr and Fe2 atoms. In (**b**)–(**d**), the band change of Fe2 atoms near the Γ point is indicated by black arrows.

the Fermi level. However, depending on stacking, the position of the spin-down CBM of Cr bands close to the Fermi level varies. The origin of the band alignment based on stacked structures is shown in Fig. 5. The relative band alignment between the FGT and CGT layers before and after stacking is shown in Fig. 5a. Before stacking, the calculated work function of pristine ML CGT, 4.33 eV, is slightly larger than that of pristine ML FGT, 4.08 eV. After stacking, atomic and electronic rearrangements occur, especially near the interface. The electron transfer from the FGT to CGT layers causes an n-type CGT layer to be formed. When the work function of the metal is less than that of the n-type semiconductor, band bending at the interface generates an Ohmic contact between the metal and the n-type semiconductor. Our vdW heterobilayer, on the other hand, has the vdW interlayer space without any extra bonds between the two constituent layers, resulting in an abrupt interface. There is only the interface dipole at the interface, which is dictated by electron distributions. The interface dipole is defined by the associated effective potential difference at the interface, δV_{eff}. The electrostatic potential difference between the vacuum levels of the FGT and CGT layers in the heterobilayer can be used to determine δV_{eff}, which is reported in Table 2. In addition, δV_{eff} is compared with that calculated using the electron density difference, and the relationship between δV_{eff} and electron transfer is explored in Fig. 6.

The band edges of the n-type CGT layer in the heterobilayer were computed to quantify the band alignment. The spin-up (red) and -down (blue) bands of E_L projected on a Cr atom are shown in the left panel of Fig. 5b, with color intensity according to the projection magnitude. Colored arrows indicate the CBM ($E^{\mathrm{CGT}}_{\mathrm{C},\uparrow,\downarrow}$) and VBM ($E^{\mathrm{CGT}}_{\mathrm{V},\uparrow,\downarrow}$) of the original Cr bands relative to the Fermi level. The CGT layer's schematic band edges are shown in the right panel of Fig. 5b. In metal/n-type semiconductor heterostructures, the n-type spin-up and spin-down band edges are specified as $\Delta_{n,\uparrow,\downarrow} = E^{\mathrm{CGT}}_{\mathrm{C},\uparrow,\downarrow} - E_{\mathrm{F}}$. In metal/$p$-type semiconductor heterostructures, the p-type spin-up and spin-down band edges are expressed as $\Delta_{p,\uparrow,\downarrow} = E_{\mathrm{F}} - E^{\mathrm{CGT}}_{\mathrm{V},\uparrow,\downarrow}$. Because $E^{\mathrm{CGT}}_{\mathrm{V},\uparrow} = E^{\mathrm{CGT}}_{\mathrm{V},\downarrow}$ in our case, $\Delta_{p,\uparrow} = \Delta_{p,\downarrow}$. The effective bandgap in the CGT layer can be described as $E^{\mathrm{CGT}}_{\mathrm{g}} = \Delta_{n,\downarrow} + \Delta_{p,\uparrow,\downarrow}$ even if it is not a genuine bandgap owing to the metal wave function tail of the FGT layer up to the Fermi level. The band edges of the CGT layer and δV_{eff} with respect to the various stacked structures are shown in Fig. 5c, and the estimated values for the band edges and $E^{\mathrm{CGT}}_{\mathrm{g}}$ are summarized in Table 2. According to Fig. 5c, the variations in band edges and δV_{eff} across different stacked structures are similar, suggesting a significant correlation. For example, the magnitude order in $\Delta_{n,\uparrow,\downarrow}$ is $E_I > E_L > E_H$, which is the same as in δV_{eff}. In all the stacked structures, $\Delta_{p,\uparrow,\downarrow}$ is larger than $\Delta_{n,\downarrow}$, confirming the n-type CGT, and the biggest variation in band edges across different structures is roughly 0.1 eV.

To study the spin/electron transfer and δV_{eff} derived from the electron density difference, the spin-resolved valence electron density difference $\delta\rho_{\uparrow,\downarrow}(z) = \rho_{\mathrm{HB}\uparrow,\downarrow}(z) - \rho_{\mathrm{FGT}\uparrow,\downarrow}(z) - \rho_{\mathrm{CGT}\uparrow,\downarrow}(z)$ was computed. Here,

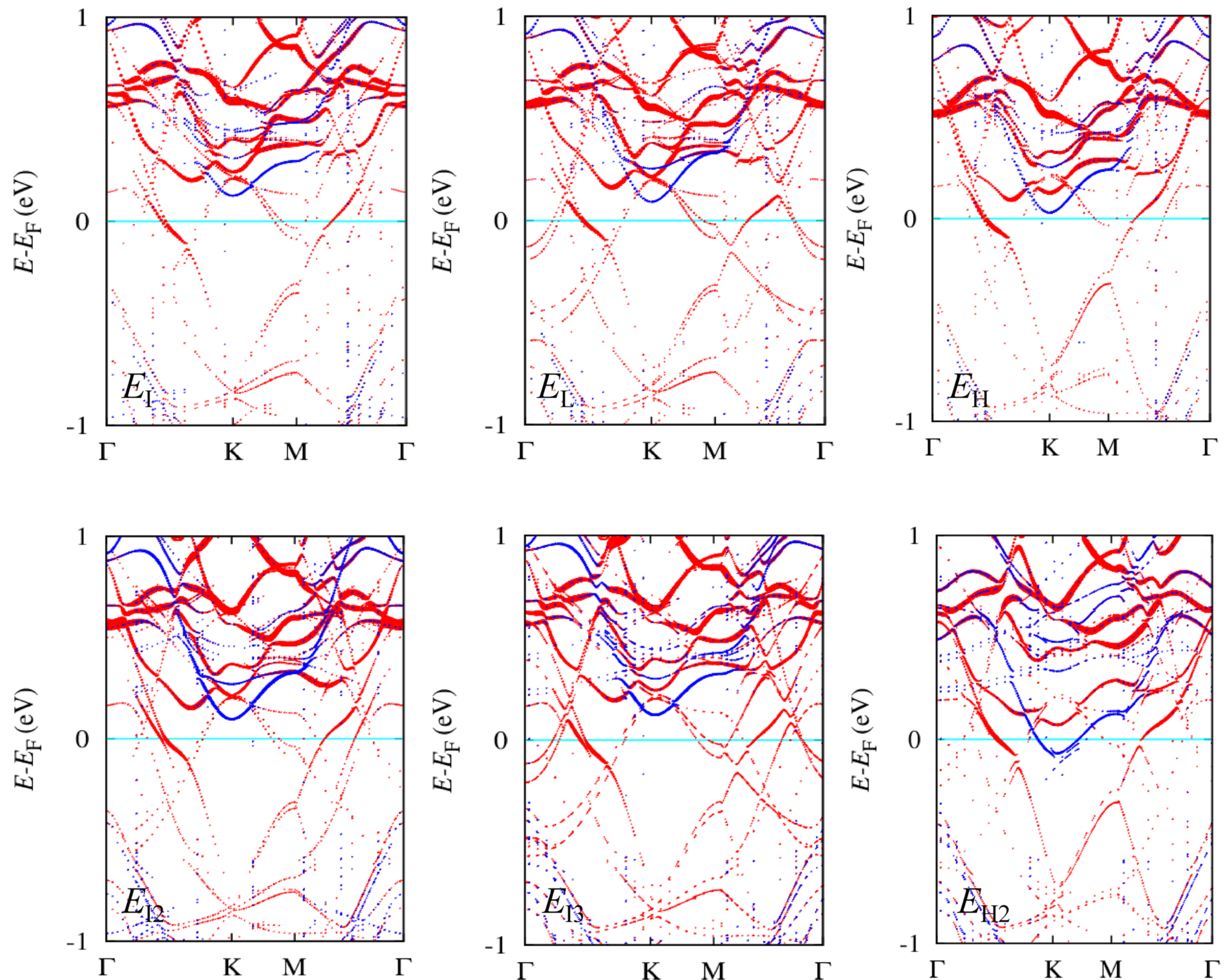

Figure 4. Band structures projected on a Cr atom for various stacked structures. The band structures are obtained by the noncollinear PBE + U + SOC method (U = 3.5 eV and J = 1.0 eV applied to Cr 3d orbitals). The red (blue) color is for spin-up (spin-down) bands; the color intensity corresponds to the projection magnitude.

$\rho_{HB\uparrow,\downarrow}(z)$,$\rho_{FGT\uparrow,\downarrow}(z)$, and $\rho_{CGT\uparrow,\downarrow}(z)$ are the spin-dependent in-plane-averaged electron densities of the heterobilayer, FGT-only, and CGT-only systems. In the case of FM heterobilayer, $\delta\rho_{\uparrow,\downarrow}$ (top panel in Fig. 6b) illustrates that the spin-up density transfers from the FGT to CGT layers, and the spin-down density transfers from the CGT to FGT layers, resulting in the effective electron density difference (black dotted lines,$\delta\rho_{\text{eff}}(z) = \delta\rho_{\uparrow}(z) + \delta\rho_{\downarrow}(z)$). A considerable electron transfer from Fe2 atoms to Cr atoms is observed in the atomic-structure figure via the bonding between Fe2 atoms and interface Te_{FGT} atoms, via the vdW spacing between interface Te_{FGT} atoms and interface Te_{CGT} atoms, and via the bonding between interface Te_{CGT} atoms and Cr atoms. Whereas the electron transfer from Fe1 atoms to Cr atoms is absent due to no direct bonding between Fe1 atoms and interface Te_{FGT} atoms. This electron-transfer pathway explains the hybridized band between Cr atoms and Fe2 atoms. In the interface region, the interface dipole appears as electron depletion and accumulation, represented by + and − signs, respectively, resulting in an effective electric field and a potential difference at the interface.

Specifically, the one-dimensional Gauss law can be used to compute the effective electric field, $E_{\text{eff}}(z)$, and effective potential difference, $\delta V_{\text{eff}}(z)$, at the interface, as illustrated in the middle panel of Fig. 6b. $Q_{in} = \int_{z0}^{z}\delta\rho_{\text{eff}}(z)dz$ gives the electron density inside the gray dashed box in the top panel, where z_0 is an arbitrary point z at the left side vacuum outside the FGT layer. Because the electric field at the left side vacuum is zero, $E_{\text{eff}}(z) = Q_{\text{in}}(z)(\varepsilon_r\varepsilon_o)^{-1}$ gives the electric field at location z, where ε_o is the vacuum permittivity, and ε_r is the position-dependent relative permittivity. Since ε_r is around 1.0, 13.50, and ∞ in the vacuum, CGT, and FGT layers, respectively, the effective electric field exists only at the interface between the two layers. Finally, $\delta V_{\text{eff}}(z)$ for electrons at the interface may be calculated using $\delta V_{\text{eff}}(z) = -\int_0^z E_{\text{eff}}(z)dz$; further, it is verified that $\delta V_{\text{eff}}(z)$ equals the sum of $\delta V_{\text{eff},\uparrow}(z)$ and $\delta V_{\text{eff},\downarrow}(z)$. The Gauss law yields δV_{eff} values (V_o in Fig. 6b) of 0.28 eV, 0.32 eV, and 0.37 eV for E_H, E_L, and E_I, respectively, which are extremely similar to the electrostatic potential differences of 0.28 eV, 0.31 eV, and 0.35 eV, respectively. Notably, the general signs for E_{eff} and δV_{eff} defined for a positive charge are the inverse of those defined for the electron in this work.

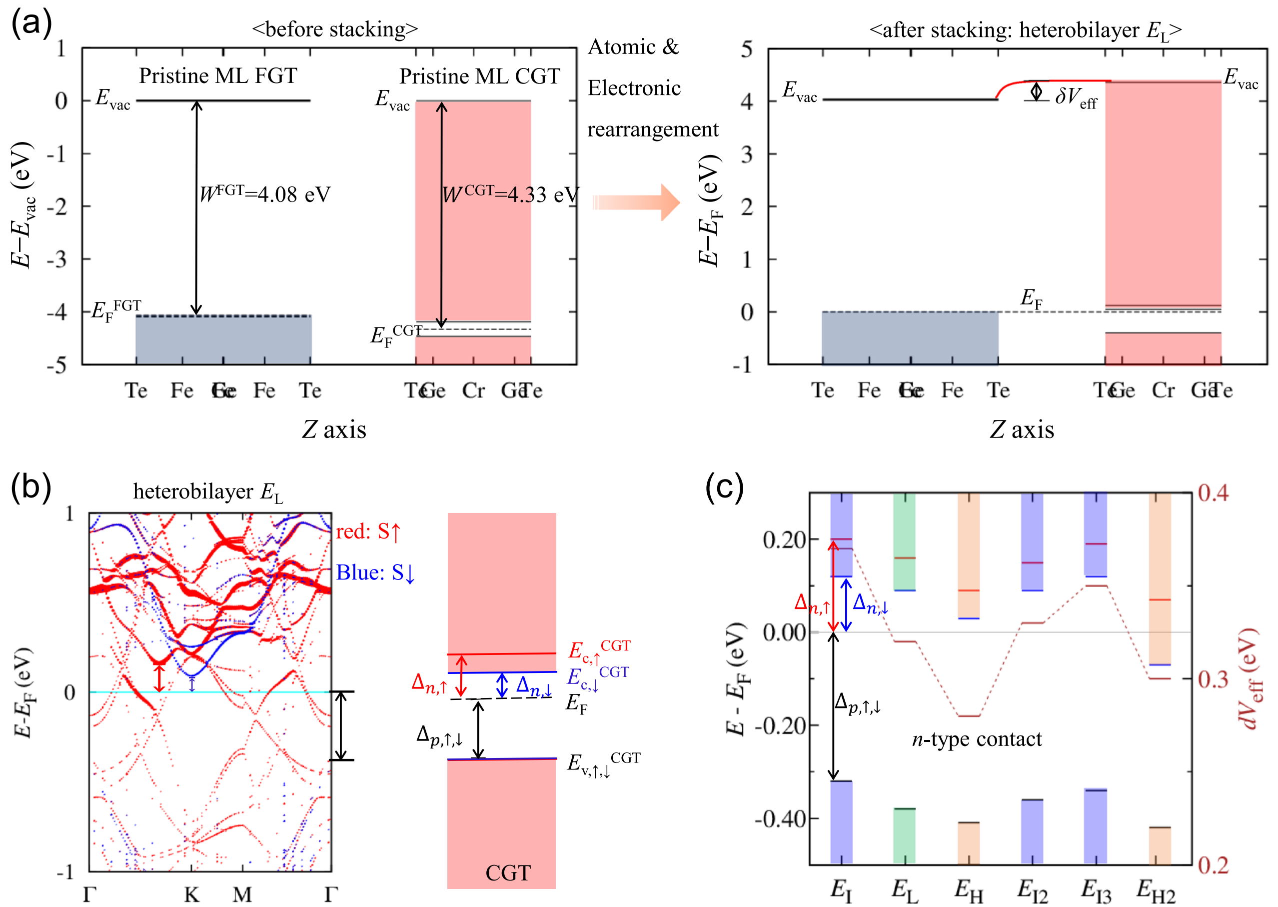

Figure 5. (**a**) Relative band alignment of the FGT and CGT layers before (left panel) and after stacking (right panel). Right after stacking, atomic and electronic rearrangements occur. E_{vac} and E_F denote the vacuum and Fermi levels, respectively. The effective potential difference, δV_{eff}, is noted at the interface. (**b**) Band structures for E_L (left panel) and schematic band edges of the CGT layer in the heterobilayer (right panel). The spin-up (red) and spin-down (blue) bands are projected onto a Cr atom; the color intensity corresponds to the projection magnitude. The *n*-type (Δ_n), and *p*-type (Δ_p) band edges are indicated by colored arrows. (**c**) Band edges of the CGT layer and effective potential difference, δV_{eff}, depending on the stacked structures.

	d_{inter} (Å)	$\Delta_{n,\uparrow}$(eV)	$\Delta_{n,\downarrow}$(eV)	$\Delta_{p,\uparrow,\downarrow}$(eV)	E_g^{CGT} (eV)	δV_{eff} (eV)
E_I	3.39	0.20	0.12	0.32	0.44	0.35
E_L	3.22	0.16	0.09	0.38	0.47	0.31
E_H	3.78	0.09	0.03	0.41	0.44	0.28
E_{I2}	3.33	0.15	0.09	0.36	0.45	0.33
E_{I3}	3.31	0.19	0.12	0.34	0.46	0.35
E_{H2}	3.71	0.07	−0.07	0.42	0.39	0.30

Table 2. Spin-dependent band edges $\Delta_{n,\uparrow,\downarrow}$ and $\Delta_{p,\uparrow,\downarrow}$, the effective bandgap of the CGT layer, E_g^{CGT}, and effective potential difference, δV_{eff}, obtained by the electrostatic potential difference between the vacuum levels of the FGT and CGT layers in the FM heterobilayer.

The spin variation ($\Delta\rho_{\uparrow,\downarrow} = \rho_{HB,\uparrow,\downarrow} - \rho_{1L,\uparrow,\downarrow}$) and the charge variation ($\Delta\rho = \Delta\rho_\uparrow + \Delta\rho_\downarrow$) per single layer were quantitatively investigated using the spin-dependent Mulliken electron differences at the atomic sites, as shown in the bottom panel of Fig. 6b. The spin-up electron in the FGT layer moves to the spin-up electron in the CGT layer by 0.10 e. In contrast, the spin-down electron in the CGT layer moves to the spin-down electron in the FGT layer by 0.05 e, resulting in a 0.05 e effective spin-up electron transfer from FGT to CGT. Also, the magnetic moment variation per single layer, i.e., $\Delta\rho_\uparrow - \Delta\rho_\downarrow$ is $\Delta m_{FGT} = -0.15\ \mu_B$ and $\Delta m_{CGT} = 0.15\ \mu_B$. In addition, the magnetic moment variation by the atomic site (δm, solid black square) demonstrates that magnetic moments are slightly larger at Cr sites and slightly smaller at Fe2 sites than those of a single layer. The spin-down variation (blue open circle) contributes more to the magnetic moment changes at the Cr and Fe2 sites than the spin-up variation (red open circle).

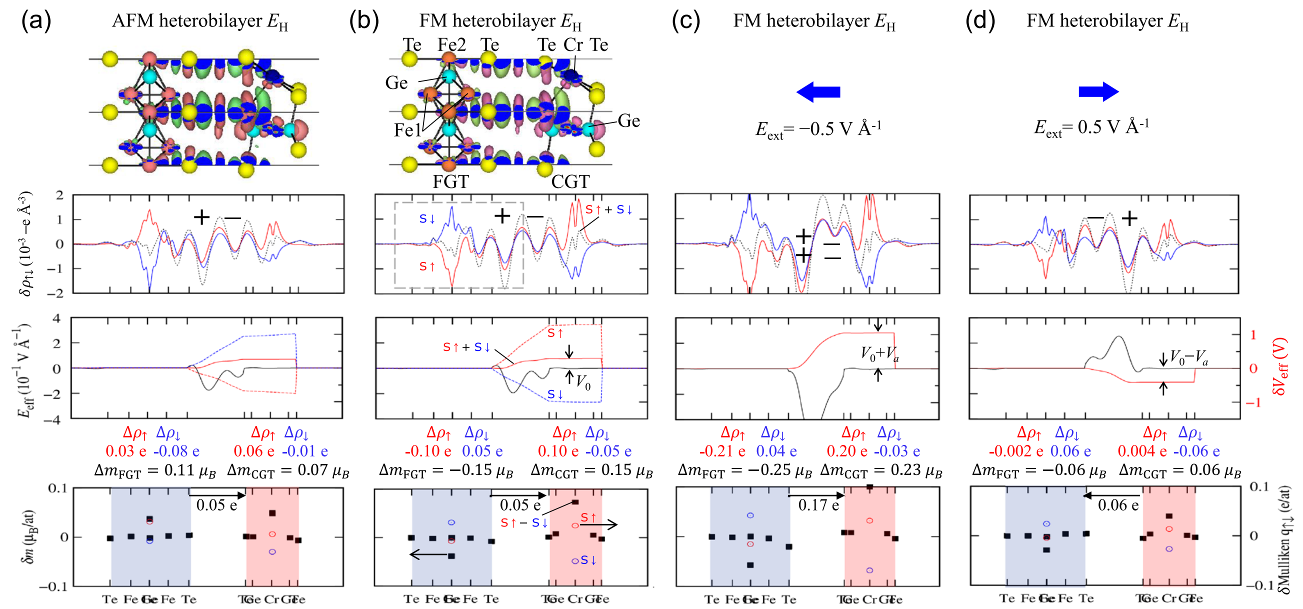

Figure 6. In-plane averaged spin-dependent electron density difference ($\delta\rho_{\uparrow,\downarrow}(z) = \rho_{HB\uparrow,\downarrow}(z) - \rho_{FGT\uparrow,\downarrow}(z) - \rho_{CGT\uparrow,\downarrow}(z)$, top panels), effective electric field, E_{eff}, effective potential difference, δV_{eff} (middle panels), magnetic moment variation ($\delta m(z) = m_{HB}(z) - m_{FGT}(z) - m_{CGT}(z)$), and spin-dependent Mulliken electron difference (bottom panels) of (**a**) the AFM FGT/CGT heterobilayer, (**b**) FM heterobilayer, (**c**) FM heterobilayer in a − 0.5 VÅ^{-1} negative electric field, and (**d**) FM heterobilayer in a 0.5 VÅ^{-1} positive electric field. The *x*-tics represent the *z*-components of atomic positions. The effective electron density difference ($\delta\rho_{eff}(z) = \delta\rho_\uparrow(z) + \delta\rho_\downarrow(z)$) is indicated by black dotted lines in the top panel. On the atomic structures in (**a**) and (**b**), the effective electron density difference with electron accumulation (magenta) and depletion (green) is depicted. The + and − symbols represent the electron depletion and accumulation at the interface in the top panel, respectively. The general signs of E_{eff} and δV_{eff} for the positive charge are opposite to them calculated for the electron in this study. $\Delta\rho_{\uparrow\downarrow}$ denotes the spin-dependent total electron density difference per single layer in the heterobilayer, and Δm represents the total magnetic moment variation per single layer. The red and blue open circles at Fe2 and Cr atoms indicate the spin-up and spin-down Mulliken electron differences, respectively.

On the other hand, the FGT layer's $\delta\rho_{\uparrow,\downarrow}$ in the AFM heterobilayer, as illustrated in the top panel of Fig. 6a, is reversed compared to that in the FM heterobilayer due to the FGT layer's reversed spin-up and spin-down bands in the AFM heterobilayer. However, the electron distribution at the interface in the AFM heterobilayer is identical to that in the FM heterobilayer, resulting in similar E_{eff} and δV_{eff}. As demonstrated in the atomic-structure figure in Fig. 6a, the practical electron-transfer pathway in the AFM heterobilayer is comparable to that in the FM heterobilayer. According to the quantitative spin variation per single layer, complex spin transfer between FGT and CGT results in a 0.05 e effective electron transfer from FGT to CGT. Also, the magnetic moment variation per single layer is $\Delta m_{FGT} = 0.11\ \mu_B$ and $\Delta m_{CGT} = 0.07\ \mu_B$. The magnetic moments of both the Cr and Fe2 sites are slightly larger than those of a single layer.

Electrostatic gating effect. This study considers positive and negative electric fields within 0.5 VÅ^{-1}, perpendicular to the in-plane direction. When utilizing the PBE + U + SOC method with U = 3.5 eV and J = 1.0 eV to compare the total energies of the FM and AFM E_H, E_I, and E_L structures concerning the external electric field, FM structures are always more stable than AFM structures, as shown in Fig. 7a. Figure 6c,d show the spin/electron transfer for the FM E_H structure. We show only E_H results because the main effect of electrostatic gating on all stacked structures is almost comparable. Our results show that the external electric field mainly modulates the spin-majority spin transfer between FGT and CGT. As shown in Fig. 6c, the variation of $\delta\rho_{\uparrow,\downarrow}$ increases when a negative electric field of − 0.5 VÅ^{-1} is introduced. Quantitatively, the spin-up electron moves from FGT to CGT by 0.21 e, whereas the spin-down electron moves from CGT to FGT by 0.03 e, resulting in a 0.17 e effective spin-up electron transfer from FGT to CGT. As a result, the magnetic moment variation per single layer increases, with $\Delta m_{FGT} = -0.25\ \mu_B$ and $\Delta m_{CGT} = 0.23\ \mu_B$, respectively. More enhanced δm at Cr sites and more reduced δm at Fe2 sites are also induced by the negative electric field. In the interface region, the negative electric field promotes electron depletion (++) and accumulation (−−), resulting in larger E_{eff} and δV_{eff} ($V_o + V_a$, where V_a = 0.76 eV in Fig. 6c).

In contrast, the variation of $\delta\rho_{\uparrow,\downarrow}$ decreases under a positive electric field of 0.5 VÅ^{-1}, as shown in Fig. 6d Consequently, the spin-up electron transfer is relatively tiny, whereas the spin-down electron transfer from CGT to FGT is 0.06 e, resulting in a 0.06 e effective spin-down electron transfer from the CGT to FGT layers. This spin transfer results in less increased and decreased δm at Cr and Fe2 sites, respectively, and reduces the magnetic

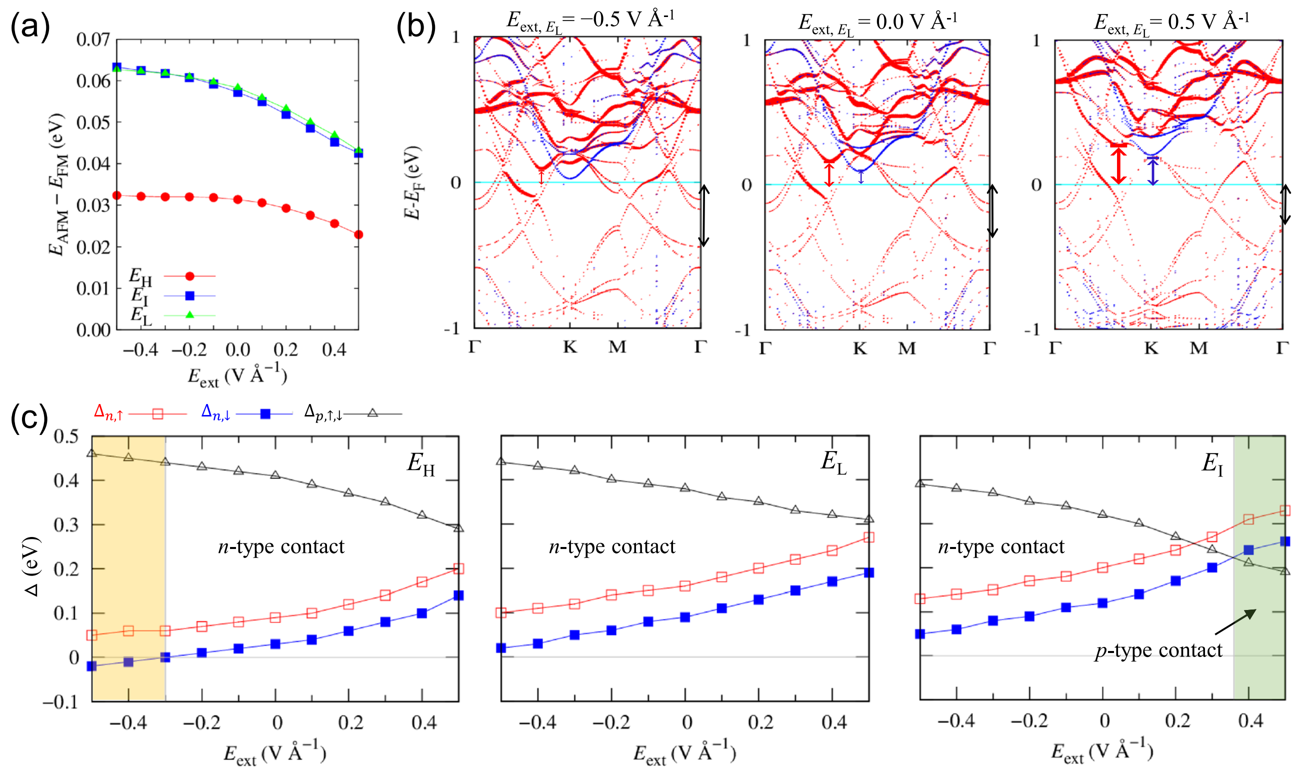

Figure 7. (**a**) Total energy difference between FM and AFM spin alignments between the FGT and CGT layers of E_H, E_I, and E_L heterobilayers with respect to the external electric field. (**b**) Band structures under the external electric field of − 0.5 VÅ^{-1} (left), 0 VÅ^{-1} (middle), and 0.5 VÅ^{-1} (right) for E_L structure. The spin-up (red) and spin-down (blue) bands are projected onto a Cr atom; the color intensity corresponds to the projection magnitude. The band-edge magnitudes relative to the Fermi level are indicated by colored arrows. (**c**) Spin-dependent n-type ($\Delta_{n\uparrow\downarrow}$) and p-type ($\Delta_{p\uparrow\downarrow}$) band-edge changes as a function of external electric field for E_H (left panel), E_L (middle panel), and E_I (right panel) heterobilayers.

moment variation per single layer. The positive electric field, especially in the interface region, generates even the opposite electron distribution, revealing the opposite action of the negative electric field. In particular, E_{eff} and δV_{eff} ($V_o - V_a$, where $V_a = 0.70$ eV in Fig. 6d) at the interface have the opposite sign.

The FGT/CGT heterobilayer is analogous to a Schottky diode in device performance, except for the opposite electron distribution in the interface. In a Schottky diode depletion zone, electron accumulation occurs near the metal, and electron depletion occurs near the n-type semiconductor. However, the electron distribution in our heterobilayer is reversed. A negative electric field to the heterobilayer, i.e., reverse bias, is achieved by connecting the battery's positive terminal to CGT and the negative terminal to FGT. The positive terminal to CGT allows FGT's electrons to migrate more to CGT, resulting in a stronger interface dipole (middle panel in Fig. 6c) and CGT's lower energy-band shift relative to the Fermi level. Furthermore, as illustrated in the left panel of Fig. 7b, the CGT's lower energy-band shift defines narrower n-type band edges but wider p-type band edges.

In contrast, a positive electric field, i.e., forward bias, is achieved by connecting the battery positive terminal to FGT and the negative terminal to CGT. The positive terminal to FGT causes CGT's electrons to move to FGT, resulting in a smaller or inverted interface dipole (middle panel in Fig. 6d). On the other hand, the negative terminal to CGT leads to the CGT's higher energy-band shift relative to the Fermi level. Furthermore, as shown in the right panel of Fig. 7b, the CGT's higher energy-band shift sets wider n-type band edges but narrower p-type band edges.

Figure 7c illustrates how the band edges change with the external electric field. As the external electric field increases, n-type band edges widen, and p-type band edges narrow, regardless of the stacked structures of E_H, E_I, and E_L. However, slightly different band-edge values depending on the stacked structures cause differences in the contact type as the external electric field changes. In the E_L heterobilayer, the n-type contact is maintained in the range of − 0.5 VÅ^{-1} to 0.5 VÅ^{-1}. In the E_H heterobilayer, the n-type contact changes to a particular contact ($\Delta_{n,\downarrow} < 0$) below − 0.3 VÅ^{-1}. In the E_I heterobilayer, the n-type contact changes to p-type contact above 0.36 VÅ^{-1}. These differences, depending on the different stacked structures, originate from the different initial potential differences (δV_{eff} when there is no external electric field) due to different asymmetric interface structures (Supplementary Information).

Conclusions

We presented the structural, electronic, and magnetic properties of layered FGT/CGT twisted moiré heterobilayers and the electrostatic gating effect. Our results show that the moiré heterobilayer with a twist angle of 30° is an FM metal with an *n*-type CGT layer regardless of various stacked structures. In the spin transfer of the FM heterobilayer, an effective spin-up electron transfer occurs from FGT to CGT. Furthermore, the spin-up hybridized bands between Cr and Fe2 atoms crossing the Fermi level are found only in the FM heterobilayer, not in the AFM heterobilayer, independent of stacking. It also turns out that the band alignment of the CGT layer is explained by the effective potential difference at the interface. Our findings further reveal that, in the FM heterobilayer, the external electric field regulates the spin-up electron transfer between the FGT and CGT layers and affects the band edges of the CGT layer. Our study could provide helpful information for understanding the effects of stacking, spin alignment, spin transfer, and electrostatic gating in the magnetic 2D vdW metal/semiconductor heterobilayer.

Data availability

All data generated or analyzed during this study are included in this published article.

Received: 17 January 2022; Accepted: 9 March 2022
Published online: 24 March 2022

References

1. Padilha, J. E., Fazzio, A. & da Silva, A. J. R. Van der Waals heterostructure of phosphorene and graphene: Tuning the Schottky barrier and doping by electrostatic gating. *Phys. Rev. Lett.* **114**, 066803 (2015).
2. Wang, Y. *et al.* Does p-type ohmic contact exist in WSe_2-metal interfaces?. *Nanoscale* **8**, 1179 (2016).
3. Farmanbar, M. & Brocks, G. Controlling the Schottky barrier at MoS_2/metal contacts by inserting a BN monolayer. *Phys. Rev. B* **91**, 161304 (2015).
4. Wang, Y. *et al.* Van der Waals contacts between three-dimensional metals and two-dimensional semiconductors. *Nature* **568**, 70 (2019).
5. Ding, X. *et al.* NbS_2: A promising p-type ohmic contact for two-dimensional materials. *Phys. Rev. Appl.* **12**, 064061 (2019).
6. Lince, J. R., Carré, D. J. & Fleischauer, P. D. Schottky-barrier formation on a covalent semiconductor without Fermi-level pinning: The metal-MoS_2(0001) interface. *Phys. Rev. B* **36**, 1647 (1987).
7. Popov, I., Seifert, G. & Tománek, D. Designing electrical contacts to MoS_2 monolayers: A computational study. *Phys. Rev. Lett.* **108**, 156802 (2012).
8. Zhong, D. *et al.* Van der Waals engineering of ferromagnetic semiconductor heterostructures for spin and valleytronics. *Sci. Adv.* **3**, e1603113 (2017).
9. Albarakati, S. *et al.* Antisymmetric magnetoresistance in van der Waals Fe_3GeTe_2/graphite/Fe_3GeTe_2 trilayer heterostructures. *Sci. Adv.* **5**, eaaw0409 (2019).
10. Li, X. *et al.* Spin-dependent transport in van der Waals magnetic tunnel junctions with Fe_3GeTe_2 electrodes. *Nano Lett.* **19**, 5133 (2019).
11. Tang, C., Zhang, L., Sanvito, S. & Du, A. Electric-controlled half-metallicity in magnetic van der Waals heterobilayer. *J. Mater. Chem. C* **8**, 7034 (2020).
12. Zhai, B., Du, J., Li, X., Xia, C. & Wei, Z. Two-dimensional ferromagnetic materials and related van der Waals heterostructures: A first-principle study. *J. Semicond.* **40**, 081509 (2019).
13. Li, H., Xu, Y. K., Cheng, Z. P., He, B. G. & Zhang, W. B. Spin-dependent Schottky barriers and vacancy-induced spin-selective ohmic contacts in magnetic vdW heterostructures. *Phys. Chem. Chem. Phys.* **22**, 9460 (2020).
14. Shabani, S. *et al.* Deep moiré potentials in twisted transition metal dichalcogenide bilayers. *Nat. Phys.* **17**, 720 (2021).
15. Weston, A. *et al.* Atomic reconstruction in twisted bilayers of transition metal dichalcogenides. *Nat. Nanotechnol.* **15**, 592 (2020).
16. Rosenberger, M. R. *et al.* Twist angle-dependent atomic reconstruction and moiré patterns in transition metal dichalcogenide heterostructures. *ACS Nano* **14**, 4550 (2020).
17. Deng, Y. *et al.* Gate-tunable room-temperature ferromagnetism in two-dimensional Fe_3GeTe_2. *Nature* **563**, 94 (2018).
18. Liu, S. *et al.* Wafer-scale two-dimensional ferromagnetic Fe_3GeTe_2 thin films grown by molecular beam epitaxy. *NPJ 2D Mater. Appl.* **1**, 30 (2017).
19. Tan, C. *et al.* Hard magnetic properties in nanoflake van der Waals Fe_3GeTe_2. *Nat. Commun.* **9**, 1554 (2018).
20. Fei, Z. *et al.* Two-dimensional itinerant ferromagnetism in atomically thin Fe_3GeTe_2. *Nat. Mater.* **17**, 778 (2018).
21. Gong, C. *et al.* Discovery of intrinsic ferromagnetism in two-dimensional van der Waals crystals. *Nature* **546**, 265 (2017).
22. Zhang, X. *et al.* Magnetic anisotropy of the single-crystalline ferromagnetic insulator $Cr_2Ge_2Te_6$. *Jpn. J. Appl. Phys.* **55**, 033001 (2016).
23. Zhuang, H. L., Kent, P. R. C. & Hennig, R. G. Strong anisotropy and magnetostriction in the two-dimensional Stoner ferromagnet Fe_3GeTe_2. *Phys. Rev. B* **93**, 134407 (2016).
24. Johansen, Ø., Risinggård, V., Sudbø, A., Linder, J. & Brataas, A. Current control of magnetism in two-dimensional Fe_3GeTe_2. *Phys. Rev. Lett.* **122**, 217203 (2019).
25. Lin, X. & Ni, J. Layer-dependent intrinsic anomalous Hall effect in Fe_3GeTe_2. *Phys. Rev. B* **100**, 085403 (2019).
26. Park, S. Y. *et al.* Controlling the magnetic anisotropy of the van der Waals ferromagnet Fe_3GeTe_2 through hole doping. *Nano Lett.* **20**, 95 (2020).
27. Carteaux, V., Brunet, D., Ouvrard, G. & Andre, G. Crystallographic, magnetic and electronic structures of a new layered ferromagnetic compound $Cr_2Ge_2Te_6$. *J. Phys. Condens. Matter* **7**, 69 (1995).
28. Hao, Z. *et al.* Atomic scale electronic structure of the ferromagnetic semiconductor $Cr_2Ge_2Te_6$. *Sci. Bull.* **63**, 825 (2018).
29. Suzuki, M. *et al.* Coulomb-interaction effect on the two-dimensional electronic structure of the van der Waals ferromagnet $Cr_2Ge_2Te_6$. *Phys. Rev. B* **99**, 161401 (2019).
30. Li, Y. F. *et al.* Electronic structure of ferromagnetic semiconductor $CrGeTe_3$ by angle-resolved photoemission spectroscopy. *Phys. Rev. B* **98**, 125127 (2018).
31. Ji, H. *et al.* A ferromagnetic insulating substrate for the epitaxial growth of topological insulators. *J. Appl. Phys.* **114**, 114907 (2013).
32. Fang, Y., Wu, S., Zhu, Z. Z. & Guo, G. Y. Large magneto-optical effects and magnetic anisotropy energy in two-dimensional $Cr_2Ge_2Te_6$. *Phys. Rev. B* **98**, 125416 (2018).
33. Siberchicot, B., Jobic, S., Carteaux, V., Gressier, P. & Ouvrard, G. Band structure calculations of ferromagnetic chromium tellurides $CrSiTe_3$ and $CrGeTe_3$. *J. Phys. Chem.* **100**, 5863 (1996).
34. Li, X. & Yang, J. $CrXTe_3$ (X = Si, Ge) nanosheets: Two dimensional intrinsic ferromagnetic semiconductors. *J. Mater. Chem. C* **2**, 7071 (2014).

35. Sivadas, N., Daniels, M. W., Swendsen, R. H., Okamoto, S. & Xiao, D. Magnetic ground state of semiconducting transition-metal trichalcogenide monolayers. *Phys. Rev. B* **91**, 235425 (2015).
36. Kang, S., Kang, S. & Yu, J. Effect of coulomb interactions on the electronic and magnetic properties of two-dimensional $CrSiTe_3$ and $CrGeTe_3$ materials. *J. Electron. Mater.* **48**, 1441 (2019).
37. Menichetti, G., Calandra, M. & Polini, M. Electronic structure and magnetic properties of few-layer $Cr_2Ge_2Te_6$: The key role of nonlocal electron-electron interaction effects. *2D Mater.* **6**, 045042 (2019).
38. Lin, Z. *et al.* Pressure-induced spin reorientation transition in layered ferromagnetic insulator $Cr_2Ge_2Te_6$. *Phys. Rev. Mater.* **2**, 051004 (2018).
39. Wang, K. *et al.* Magnetic and electronic properties of $Cr_2Ge_2Te_6$ monolayer by strain and electric-field engineering. *Appl. Phys. Lett.* **114**, 092405 (2019).
40. Liu, Y., Huang, Y. & Duan, X. Van der Waals integration before and beyond two-dimensional materials. *Nature* **567**, 323 (2019).
41. Schulman, D. S., Arnold, A. J. & Das, S. Contact engineering for 2D materials and devices. *Chem. Soc. Rev.* **47**, 3037 (2018).
42. Zhang, F., Li, W., Ma, Y., Tang, Y. & Dai, X. Tuning the Schottky contacts at the graphene/WS_2 interface by electric field. *RSC Adv.* **7**, 29350 (2017).
43. Wu, J. *et al.* High electron mobility and quantum oscillations in non-encapsulated ultrathin semiconducting Bi_2O_2Se. *Nat. Nanotechnol.* **12**, 530 (2017).
44. Troullier, N. & Martins, J. L. Efficient pseudopotentials for plane-wave calculations. *Phys. Rev. B* **43**, 1993 (1991).
45. Sánchez-Portal, D., Ordejón, P., Artacho, E. & Soler, J. M. Density-functional method for very large systems with LCAO basis sets. *Int. J. Quantum Chem.* **65**, 453 (1997).
46. Lichtenstein, A. I., Anisimov, V. I. & Zaanen, J. Strong interactions: Orbital ordering. *Phys. Rev. B* **52**, 5467 (1995).
47. Lee, N. *et al.* Antiferromagnet-based spintronic functionality by controlling isospin domains in a layered perovskite iridate. *Adv. Mater.* **30**, 1805564 (2018).
48. Ko, E. & Son, Y. W. First-principles study on effects of local Coulomb repulsion and Hund's coupling in ferromagnetic semiconductor $CrGeTe_3$. *J. Appl. Phys.* **128**, 123901 (2020).
49. Yankowitz, M. *et al.* Emergence of superlattice Dirac points in graphene on hexagonal boron nitride. *Nat. Phys.* **8**, 382 (2012).
50. Tang, S. *et al.* Precisely aligned graphene grown on hexagonal boron nitride by catalyst free chemical vapor deposition. *Sci. Rep.* **3**, 2666 (2013).
51. Kong, X., Li, L. & Peeters, F. M. Graphene-based heterostructures with moiré superlattice that preserve the Dirac cone: A first-principles study. *J. Phys. Condens. Matter* **31**, 255302 (2019).

Acknowledgements

E. Ko was supported by an individual Grant (CG075002) at Korea Institute for Advanced Study (KIAS). E. Ko thanks Young-Woo Son and Beom Hyun Kim for useful discussions. E. Ko expresses gratitude to Sehoon Oh for assisting with developing the SIESTA code used to calculate the unfolded band structure. This work was supported by the Center for Advanced Computation at KIAS and by the KISTI Supercomputing Center with supercomputing resources, including technical support (KSC-2019-CRE-0208).

Author contributions

E.K. performed, analyzed all the calculations, and prepared the manuscript.

Competing interests

The author declares no competing interests.

Additional information

Supplementary Information The online version contains supplementary material available at https://doi.org/10.1038/s41598-022-08785-x.

Correspondence and requests for materials should be addressed to E.K.

Reprints and permissions information is available at www.nature.com/reprints.

Publisher's note Springer Nature remains neutral with regard to jurisdictional claims in published maps and institutional affiliations.

Open Access This article is licensed under a Creative Commons Attribution 4.0 International License, which permits use, sharing, adaptation, distribution and reproduction in any medium or format, as long as you give appropriate credit to the original author(s) and the source, provide a link to the Creative Commons licence, and indicate if changes were made. The images or other third party material in this article are included in the article's Creative Commons licence, unless indicated otherwise in a credit line to the material. If material is not included in the article's Creative Commons licence and your intended use is not permitted by statutory regulation or exceeds the permitted use, you will need to obtain permission directly from the copyright holder. To view a copy of this licence, visit http://creativecommons.org/licenses/by/4.0/.

© The Author(s) 2022